LAWRENCE
LIVERMORE
NATIONAL
LABORATORY

Structure of low-density nanoporous dielectrics revealed by low-vacuum electron microscopy and small-angle x-ray scattering
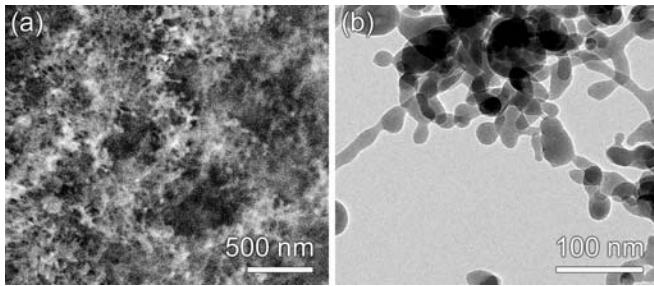
S. O. Kucheyev, M. Toth, T. F. Baumann, A. V. Hamza, J. Ilavsky, W. R. Knowles, B. L. Thiel, V. Tileli , T. van Buuren, Y. M. Wang, T. M. Willey

June 9, 2006

Disclaimer

(a) 500 nm

(b) 100 nm

Graphical abstract

We use low-vacuum scanning electron microscopy to image directly the ligament and pore size and shape distributions of representative aerogels over a wide range of length scales ($\sim 10^0 - 10^5$ nm). The images are used for unambiguous, real-space interpretation of small-angle scattering data for these complex nanoporous systems.

Structure of low-density nanoporous dielectrics revealed by low-vacuum electron microscopy and small-angle x-ray scattering[**]

Sergei O. Kucheyev,* Milos Toth,[†,‡] Theodore F. Baumann,* Alex V. Hamza,* Jan Ilavsky,[§] W. Ralph Knowles,[†] Bradley L. Thiel,[‡] Vasiliki Tileli,[‡] Tony van Buuren,* Y. Morris Wang,* and Trevor M. Willey*

*Lawrence Livermore National Laboratory, Livermore, California 94550
[†]FEI Company, 29 Water Street #216-217, Newburyport, Massachusetts 01950
[‡]College of Nanoscale Science and Engineering, University at Albany-SUNY, 255 Fuller Rd, Albany, New York 12203 and
[§]Argonne National Laboratory, Argonne, Illinois 60439
(Dated: June 5, 2006)

Aerogels (AGs) are a class of ultralow-density open-cell nanoporous solids with typical porosities of $\gtrsim 90\%$ and large surface areas (typically $\gtrsim 100$ m^2 g^{-1}).[1] Particulate silica AGs — the best studied class of AGs — have the so called string-of-pearls morphology, consisting of interconnecting near-spherical nanoparticles.[1] In addition to silica, synthesis of many other AGs, mostly dielectric oxides, have been reported.[1] Such AGs often display vastly different nanoligament shapes and sizes, including near spherical particles, rods with different aspect ratios, and quasi-two-dimensional (2D) leaflets.

The shape and size of ligaments in nanoporous dielectrics are commonly studied by transmission electron microscopy (TEM). However, technologically important properties of nanoporous solids strongly depend not only on the ligament structure but also on the distribution of ligament and pore sizes (i.e., density fluctuations) and the presence of other structural inhomogeneities such as microcracks. Conventional TEM imaging does not probe such a 3D morphology.[2,3]

Other techniques commonly used to image dielectric nanomaterials are scanning electron (SEM) and atomic force (AFM) microscopy. These methods, however, face serious challenges in the case of low-density nanoporous dielectrics. Specifically, SEM imaging is compromised by severe charging under the electron beam, and conformal coating of AG nanoligaments with thin conductive films (used to suppress charging) that do not alter the surface topography is extremely challenging. In the case of AFM, it has been demonstrated by several groups[4–7] that even tapping-mode imaging of low-density AGs is plagued by a very high aspect ratio of surface features, poor mechanical properties,[8,9] and tip contamination by AG debris. Consequently, AG morphology is commonly studied by indirect methods such as nitrogen sorption and small-angle x-ray (SAXS) and neutron (SANS) scattering.[1] However, as we discuss below, information obtained from nitrogen sorption is limited, and real-space interpretation of SAXS and SANS data from complex nanoporous systems is highly model dependent.

In this paper, we demonstrate unambiguous visualization of the structure of several representative highly-insulating AGs over a wide range of length scales ($\sim 10^0 - 10^5$ nm). We use low-vacuum SEM (LVSEM), where charging is stabilized by a small amount ($\lesssim 100$ Pa) of weakly ionized gas inside the specimen chamber.[10] In particular, our results reveal the presence of large-scale pores (i.e., hundreds of nanometers in size) in some AGs and the existence of a highly-defective skin layer on otherwise crack-free monoliths for all the AGs studied. These features cannot be studied by the abovementioned techniques, and have important implications for understanding AG properties affecting their mechanical, gas/fluid diffusion, adsorption, and electronic transport behavior.[1] We use the LVSEM results to interpret SAXS curves for these complex nanoporous systems.

We studied three recently synthesized AGs with string-of-pearls (α-AlOOH), nanorod (GeO$_2$), and nanoleaflet
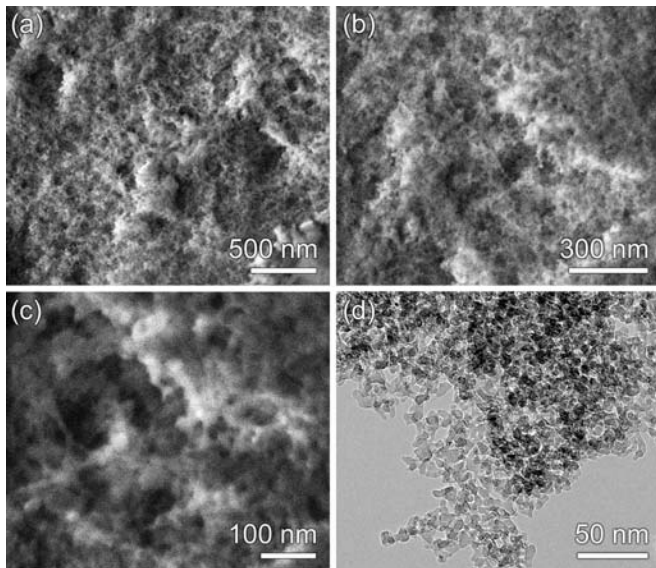
FIG. 1: Low-vacuum SEM (a-c) [$V_0 = 5$ kV, $P = 55$ Pa] and conventional bright-field TEM (d) images of a cross-section of the α-AlOOH aerogel.

FIG. 2: Low-vacuum SEM (a-c) and conventional bright-field TEM (d) images of the (exterior) surface (a-b) and a cross-section (c-d) of a γ-AlOOH aerogel monolith. Images (a) and (b) [$V_0 = 5$ kV, $P = 60$ Pa] show the same sample area under different magnifications. For image (c), $V_0 = 18$ kV and $P = 55$ Pa.

(γ-AlOOH) ligament morphologies. Table I gives a brief description of these AGs, while additional details of AG synthesis and their basic properties can be found elsewhere.[11–13]

Figures 1(a-c) show typical LVSEM images of a cross-section of the α-AlOOH AG, which has a string-of-pearls morphology.[14] Such cross sections were prepared by fracturing AG monoliths. The ligament shapes and sizes of this AG are also illustrated by a higher-magnification TEM image in Fig. 1(d). Figures 1(a-c) clearly show that the structure of this AG is nonuniform, containing pores with diameters of up to $\sim 200 - 300$ nm, which is significantly larger than an average pore size of ~ 20 nm measured by Barrett-Joyner-Halenda (BJH) nitrogen desorption analysis (see Table I). Such structural inhomogeneities cannot be observed by conventional TEM, and the BJH analysis is not sensitive to macropores with diameters $\gtrsim 200$ nm.[15]

We note that high-resolution LVSEM images in Figs. 1(a-c) do not show any evidence of charging. Such artifact-free imaging of strongly insulating nanoporous solids is challenging because of the wide pore and ligament size distributions. Indeed, during image acquisition, when the electron beam is scanned across the sample surface, the charge-up and discharge rates of neighboring volume elements are affected by the local pore structure. Hence, for artifact-free imaging, an effective charge control mechanism must respond in real time to the resulting fluctuations in charging. In LVSEM, this is achieved by ensuring that electron irradiation gives rise to net negative sample charging and by regulating the flux of gaseous ions at the sample surface.[10] The ion flux is made to self-regulate by (i) ensuring that the ion generation rate in the gas is much greater than the electron
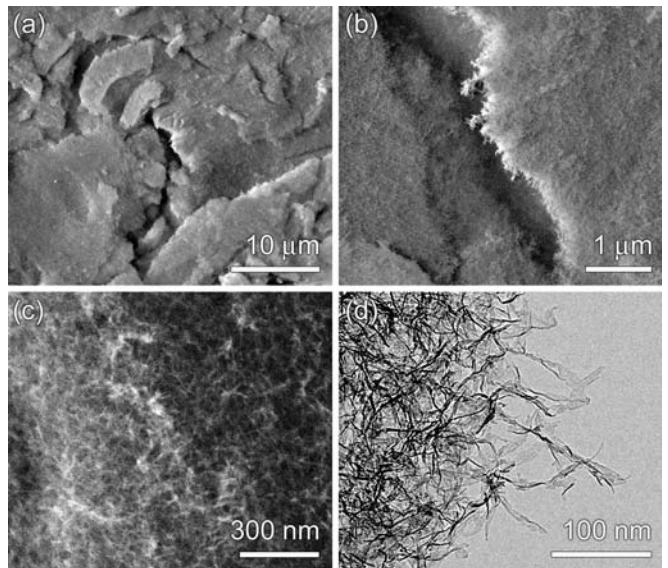
implantation rate in the sample, (ii) providing an ion sink (i.e., a grounded metal) in the vicinity of the sample surface, and (iii) setting up the electrostatic boundary conditions such that the trajectories of ions are much more sensitive to subtle electric fields at the sample surface than are the trajectories of primary beam and secondary electrons. A detailed discussion of the optimum experimental conditions required for artifact-free imaging, as presented here, can be found in Refs. 16 and 17.

The structure of the γ-AlOOH AG, with a nanoleaflet ligament morphology [see a TEM micrograph in Fig. 2(d)], is illustrated in a LVSEM image in Fig. 2(c).[14] Figure 2(c) illustrates that the γ-AlOOH AG has a more uniform pore size distribution than the α-AlOOH AG shown in Fig. 1. The morphology of the GeO_2 AG is illustrated by LVSEM and TEM images in Fig. 3.[14] This GeO_2 AG consists of a continuous network of elongated amorphous GeO_2 ligaments, $\sim 15 - 20$ nm in diameter and $\sim 50 - 200$ nm in length. Larger particles ($\sim 40 - 60$ nm in diameter) with aspect ratios $\lesssim 2$ are also clearly visible in Fig. 3. The LVSEM image in Fig. 3(a) shows that GeO_2 AGs exhibit structural inhomogeneities, with some pores as large as $\sim 200 - 400$ nm, similar to those of α-AlOOH AGs (Fig. 1).

We have also used LVSEM to image the exterior surfaces of a number of as-cast AG monoliths: α-AlOOH, γ-AlOOH, and GeO_2 AGs, described in Table I, as well as amorphous TiO_2 (Ref. 18) and β-FeOOH (Ref. 19). Interestingly, the exterior surfaces of all these AGs (i.e., the monolith skin layers) contain cracks, which are not observed in images of cross-sections. The crack size varies

TABLE I: Selected properties of the three aerogels studied. Radii of gyration (R_g) and power law slopes (α_s and α_m) obtained from standard Guinier and Porod analyses of SAXS curves are also listed.

Sample	Precursor	Morphology	Phase	Density		APD [a]	R_{g1}	R_{g2}	$-\alpha_s$	$-\alpha_m$
				(mg cm^{-3})	(%)	(nm)	(nm)	(nm)		
α-AlOOH	$Al(NO_3)_3 \bullet 9H_2O$	string-of-pearls	diaspore	135	3.97	20	5.0	50	4.0	1.8
γ-AlOOH	$AlCl_3 \bullet 6H_2O$	nanoleaflet	boehmite	48	1.41	20	2.5	20	3.8	2.1
GeO_2	$Ge(OMe)_4$	nanorod	amorphous	35	0.80	15	20	−	4.0	1.3

[a]APD = average pore diameter, measured by Barrett-Joyner-Halenda nitrogen desorption analysis in Refs. 11–13.
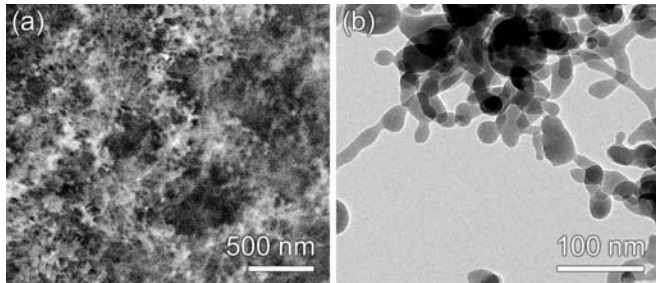

FIG. 3: Low-vacuum SEM (a) [$V_0 = 18$ kV, $P = 55$ Pa] and conventional bright-field TEM (b) images of cross-sections of the GeO_2 aerogel.

widely, from hundreds of nanometers up to tens of microns. The areal density of cracks is highly non-uniform. As an example, Figs. 2(a) and 2(b) show the morphology of the skin layer on a γ-AlOOH AG monolith, with numerous microcracks clearly visible. These cracks likely originate from gradients of tensile stresses that develop during supercritical drying. Clearly, the presence of such a highly defective skin layer on AG monoliths is crucial for a correct analysis of properties and performance of cast monolithic AGs.

Finally, we demonstrate how the information obtained from direct imaging with LVSEM and TEM can be used to interpret data measured with SAXS — currently one of the most common tools for studying AG morphology.[1] Figure 4(a) shows that SAXS intensity $I(q)$ curves for α-AlOOH, γ-AlOOH, and GeO_2 AGs are drastically different, reflecting the differences in their morphology. Values of power law exponents (α_s and α_m) and radii of gyration (R_{g1} and R_{g2}) obtained from standard Porod and Guinier analyses[20] are listed in Table I, and the corresponding linear fits and knee points in SAXS curves are shown in Fig. 4(a) by straight lines and arrows, respectively. Since scattering curves of nanoporous dielectrics are typically interpreted based on a fractal model (see, for example, Refs. 4,6,20–22), below we will use it to interpret SAXS data from Fig. 4. We note, however, that the fractal analysis of SAXS data for disordered systems is somewhat controversial: the same SAXS curves could, for example, be interpreted in terms of density fluctuations, asymmetry in the shape of ligaments, and/or large
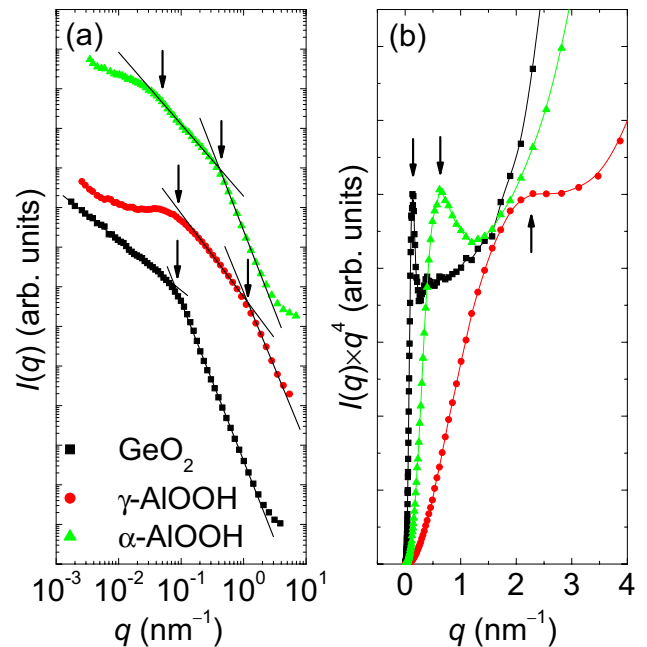

FIG. 4: Plots of SAXS intensity $I(q)$ (a) and $I(q) \times q^4$ (b) as a function of scattering vector q for α-AlOOH, γ-AlOOH, and GeO_2 aerogels. Positions of knee points in (a), related to radii of gyration, and the first maxima in (b) are indicated by arrows. For clarity, in (a), curves are offset by a factor of 100, and only every second experimental point is shown.

ligament polydispersity rather than fractals.[23–25]

In the fractal model,[20] R_{g1} and R_{g2} are related to the mean size of ligaments a and the correlation range ξ (which is roughly the fractal size), respectively. The difference in a in our AGs is also more clearly illustrated in Fig. 4(b), where $I(q) \times q^4$ versus q is plotted. The position of the first maximum in such $I(q) \times q^4$ plots is related to the mean size of scatterers in the Porod regime.[26] However, how exactly R_{g1} and R_{g2} are related to a and ξ strongly depends on the shape and size distribution of scatterers.[20–22] For a non-speculative interpretation of SAXS data, information from direct imaging methods is required. For example, values of R_{g1} from Table I translate into a mean particle diameter of $2\sqrt{5/3}R_{g1} \approx 13$ nm for the α-AlOOH AG (with roughly

spherical particles as building blocks),[20] into a mean ligament width of $2\sqrt{4/3}R_{g1} \approx 45$ nm for the GeO_2 AG (with rod-like ligaments),[24] and into a mean nanoleaflet thickness of $2R_{g1} \approx 5$ nm for the γ-AlOOH AG (with leaflet-like ligaments).[24] These numbers are consistent with microscopy data from Figs. 1 and 3, particularly given that the Guinier analysis overestimates the mean scatterer size for polydisperse systems.[22]

The slope α_s of the first high-q linear region in Fig. 4(a) describes the surface roughness of ligaments and is related to the surface fractal dimension via $D_s = \alpha_s + 6$.[20] A surface fractal dimension of 2.0 (i.e., $\alpha_s = -4$) is characteristic of a smooth (non-fractal) surface. Table I shows that α-AlOOH and GeO_2 AGs have smooth surfaces ($D_s = 2.0$), while D_s for the γ-AlOOH AG is ~ 2.2, which is consistent with a leaflet-like, irregular shape of ligaments in γ-AlOOH AGs (Fig. 2).

The slope α_m of the second power law region in Fig. 4 (at low q, between the two Guinier regimes indicated by arrows) describes the mass fractal dimension $D_m = -\alpha_m$ or the dimension of the scatterers.[20] The values of α_m given in Table I are consistent with (i) diffusion-limited cluster aggregation (DLCA) resulting in a fractal string-of-pearls morphology for α-AlOOH AGs, (ii) 2D leaflet-like ligaments for γ-AlOOH AGs, and (iii) rod-like ligaments for GeO_2 AGs. Indeed, in ideal cases of DLCA gels, thin sheets, and rods, α_m values would be 1.8, 2.0, and 1.0, respectively,[20,22] which are close to the α_m values measured (Table I).

Figure 4 and Table I also show that, while the GeO_2 AG exhibits a mass-fractal-like behavior over a very large q range of, at least, two orders of magnitude ($10^{-3} < q < 10^{-1}$ nm^{-1}), the effective mass fractal range ($\sim R_{g2}/R_{g1}$) for α-AlOOH and γ-AlOOH AGs is only about one order of magnitude. Such mass fractal ranges shorter than an order of magnitude are, however, typical for silica AGs.[1,4,6,21] In addition, inhomogeneities in the pore size distribution (resulting in density fluctuations), with the presence of large pores of $\sim 200 - 300$ nm in diameter, revealed by LVSEM for α-AlOOH and GeO_2, can explain the power law slopes in SAXS curves for $q < 5 \times 10^{-2}$ nm^{-1} for these AGs (and not for the γ-AlOOH AG, which has a more uniform structure [Fig. 2]). An accurate qualitative description of SAXS curves with a physically meaningful model for the AGs studied here is, however, challenging due to their complex morphologies.

The above results demonstrate that, in contrast to highly model-dependent interpretation of (reciprocal space) scattering data, electron microscopy provides unambiguous real-space visualization of the morphology of nanoporous dielectrics. We note, however, that the measurement of parameters such as fractal dimensions and correlation ranges for fractal solids as well as 3D correlation effects in non-fractal solids is straightforward by SAXS but is very challenging by LVSEM since pixel intensity in LVSEM images is governed by electron contrast formation mechanisms and does not necessarily scale with the height of surface features. In addition, SAXS provides information on 3D morphology statistically representative over large sample volumes ($\sim$ several mm^3), which is not readily probed by electron microscopy.

In conclusion, we have demonstrated the use of low-vacuum SEM to image directly the ligament and pore size and shape distributions of representative aerogels over a wide range of length scales ($\sim 10^0 - 10^5$ nm). As most aerogels are strong insulators with poor mechanical properties, direct studies of their structure by methods such as atomic force and conventional SEM have not proven feasible. The structural information obtained from LVSEM imaging in the present work is used for unambiguous, real-space interpretation of small-angle scattering curves for these complex nanoporous systems. Low-vacuum SEM permits imaging of both cross-sections and skin layers of nanoporous monoliths. Images of skin layers reveal the presence of microcracks which alter the properties of cast monolithic aerogels.

Experimental

Low-vacuum SEM was performed in an FEI Nova NanoSEM with water vapor as the imaging gas. High magnification secondary electron (SE) imaging of untreated, bulk AG monoliths was achieved using a recently developed magnetic-field-assisted gas cascade detector.[16,27] This detector uses the field of a magnetic immersion electron lens to induce axial and cycloidal SE oscillations inside the detector volume. The resulting magnetic confinement leads to an intense gas ionization cascade which amplifies the SE signal and generates gaseous ions. These ions are used to stabilize charging under the conditions imposed by ultra-high resolution magnetic immersion electron lenses.[16,27] Wide field width SE imaging of AG skin layers was done using a pinhole electron lens and a standard, off-axis gaseous detector.[17] Bright-field TEM imaging was performed using a Philips CM300FEG electron microscope operated at 300 kV.

Ultra-small-angle x-ray scattering measurements of monolithic samples, $\sim 5 \times 5 \times 3$ mm^3 in size, were carried out at beamline 33-ID at the Advanced Photon Source at Argonne National Laboratory. The data were collected with a double-crystal Bonse-Hart instrument. The x-ray energies were 9.5 and 11 keV, and the x-ray beam size was $\sim 2.0 \times 0.4$ mm^2. All SAXS measurements were performed at room temperature in air at ambient pressure. The slit-smeared SAXS data were corrected for background scattering, calibrated against an empty-cell blank run, and desmeared.

[1] See, for example, reviews by N. Hüsing and U. Schubert, Angew. Chem. Int. Edn Engl. **37**, 22 (1998); A. C. Pierre and G. M. Pajonk, Chem. Rev. **102**, 4243 (2002).

[2] It should be mentioned that Ruben et al.[3] have reported molecular-level visualization of the structure of particulate silica and organic AGs by high-resolution TEM which involved painstaking preparation of vertical Pt-C replicas. This state-of-the-art replication technique is, however, very labor intensive and, hence, is not suitable for convenient analysis of AG morphology.

[3] G. C. Ruben, R. W. Pekala, T. M. Tillotson, and L. W. Hrubesh, J. Mater. Sci. **27**, 4341 (1992); G. C. Ruben and R. W. Pekala, J. Non-Cryst. Sol. **186**, 219 (1995).

[4] A. Borne, C. Chevalier, J. L. Chevalier, D. Quenard, E. Elaloui, and J. Lambard, J. Non-Cryst. Sol. **188**, 235 (1995).

[5] R. W. Stark, T. Drobek, M. Weth, J. Fricke, and W. M. Heckl, Ultramicroscopy **75**, 161 (1998).

[6] C. Marliere, F. Despetis, P. Etienne, T. Woignier, P. Dieudonne, and J. Phalippou, J. Non-Cryst. Sol. **285**, 148 (2001).

[7] R. Jones, H. M. Pollock, D. Geldart, and A. Verlinden, Powder Technology **132**, 196 (2003).

[8] Low-density AGs are notoriously known for their poor mechanical properties, related to the fact that their elastic modulus decreases highly superlinearly with decreasing monolith density, with an exponent of $\sim 3 - 4$.[9]

[9] See, for example, H. S. Ma, A. P. Roberts, J. H. Prevost, R. Jullien, and G. W. Scherer, J. Non-Cryst. Sol. **227**, 127 (2000); and references therein.

[10] See, for example, a recent review by B. L. Thiel and M. Toth, J. Appl. Phys. **97**, 051101 (2005).

[11] T. F. Baumann, A. E. Gash, and J. H. Satcher, Jr., Chem. Mater. **17**, 395 (2005).

[12] S. O. Kucheyev, T. F. Baumann, Y. M. Wang, T. van Buuren, J. F. Poco, J. H. Satcher, Jr., and A. V. Hamza, Appl. Phys. Lett. **88**, 103117 (2006).

[13] S. O. Kucheyev, T. F. Baumann, C. A. Cox, Y. M. Wang, J. H. Satcher, Jr., and A. V. Hamza (unpublished).

[14] In figure captions, V_0 is electron beam accelerating voltage, and P is gas pressure inside the specimen chamber.

[15] S. J. Gregg and K. S. W. Sing, *Adsorption, Surface Area, and Porosity* (Academic, London, 1982).

[16] M. Toth, W. R. Knowles, and B. L. Thiel, Appl. Phys. Lett. **88**, 023105 (2006).

[17] M. Toth, M. R. Phillips, J. P. Craven, B. L. Thiel, and A. M. Donald, J. Appl. Phys. **91**, 4492 (2002).

[18] S. O. Kucheyev, T. van Buuren, T. F. Baumann, J. H. Satcher, Jr., T. M. Willey, R. W. Meulenberg, T. E. Felter, J. F. Poco, S. A. Gammon, and L. J. Terminello, Phys. Rev. B **69**, 245102 (2004).

[19] A. E. Gash, J. H. Satcher, Jr., and R. L. Simpson, Chem. Mater. **15**, 3268 (2003).

[20] See, for example, R.-J. Roe, *Methods of X-Ray and Neutron Scattering in Polymer Science* (Oxford University Press, New York, 2000).

[21] D. W. Schaefer and K. D. Keefer, Phys. Rev. Lett. **56**, 2199 (1986).

[22] A. Hasmy, R. Vacher, and R. Jullien, Phys. Rev. B **50**, 1305 (1994).

[23] W. Ruland, Carbon **39**, 287 (2001).

[24] B. Beaucage, J. Appl. Cryst. **28**, 717 (1995).

[25] M. Shibayama, S. Nomura, T. Hashimoto, E. L. Thomas, J. Appl. Phys. **66**, 4188 (1989).

[26] Weak intensity oscillations visible for the GeO_2 AG in Fig. 4(b) suggest a narrow size distribution of scatterers (with the ratio of the standard deviation to the mean size of $\lesssim 35\%$).[20,22]

[27] B. L. Thiel, M. Toth, R. P. M. Schroemges, J. J. Scholtz, G. van Veen, and W. R. Knowles, Rev. Sci. Instr. **77**, 033705 (2006).